

# Turbulent heat flux in the deep ocean above diffuse hydrothermal vents

Matthew J. Pruis, Susan L. Hautala, H. Paul Johnson,

Irene García Berdeal and Tor Bjorklund

*School of Oceanography, University of Washington, Seattle, WA 98195, USA*<sup>1</sup>

---

## Abstract

Turbulence data collected near diffuse hydrothermal vents on the Endeavour Segment of the Juan de Fuca Ridge reveal the processes important in turbulent heat transfer in this unusual oceanic environment. Temperature measurements obtained at the rock / water interface demonstrate that low-temperature diffuse effluent leaving the oceanic crust is highly variable. Our calculations show that this variability at the interface is quickly mixed in the near-bottom boundary layer. Velocity and temperature time series, at a measurement height of roughly 0.5 meters above the seafloor, indicate that heat and momentum flux occur at nearly the same scale. Typical turbulent eddies are 0.10 to 0.25 m in dimension, with the largest (energy containing) turbulent eddies occurring at scales of approximately 0.45 m. The turbulent eddies that are responsible for heat transfer depend mainly on the shear forcing, not thermal buoyancy. Probability distribution functions confirm that most of the heat flux occurs in intermittent events, and yield a mean heat flux value of order 4 kW/m<sup>2</sup>.

*Key words:* turbulence, hot springs, Juan de Fuca, heat flow

---

## 1 Introduction

Measurements obtained over the past few years aimed at determining the heat flux of diffuse hydrothermal vents have provided several insights into the way in which this heat is transferred into the deep ocean boundary layer. These results are not only significant for predicting the magnitude of heat transfer from this type of hydrothermal venting, but also in understanding how other biological and chemical properties are distributed in the ridge-axis environment. There are three ways in which hydrothermal fluid typically exits the seafloor; (1) focused high-temperature vents, (2) diffuse seepage of hydrothermal fluid through, or closely associated with vent structures, or (3) low-temperature, diffuse flow that occurs distant from focused vent structures. Initially, high-temperature focused vents drew the most attention, since this type of venting is easier to detect with water column surveys, and also because the focused nature of flow from the structures made it (somewhat) easier to estimate mass and energy fluxes. Even so, the scale of measurement is difficult to obtain using deep-diving submersibles and/or remotely-operated vehicles at the seafloor. Sulfide structures have been documented up to 50-m tall, and each structure may consist of several, to dozens, of individual high-temperature vent orifices (Robigou et al., 1993).

A high-temperature vent site is defined to consist of at least one *smoker* vent,  $> 215^{\circ}\text{C}$ , however the actual number may be much larger. For example, the Main Endeavour vent field (which is included in this study) consists of over

---

<sup>1</sup> Corresponding author present address: NorthWest Research Associates, 14508 NE 20th Street, Bellevue, WA 98007, USA. Tel.: 425-644-9660, ext. 311; Fax: 425-644-8422. *E-mail* : matt@nwra.com (M.J. Pruis).

one hundred individual vent orifices, and covers an area greater than  $1 \text{ km}^2$  (Delaney et al., 1992; Butterfield et al., 1994). Temperature and velocity measurements obtained within a few centimeters of focused vent orifices yield power outputs which range from less than 1 to nearly 100 MW, and effluent fluid velocities between 0.1 and 2 m/s (Little et al., 1987; Rona and Trivett, 1992; Ginster et al., 1994). Complicating the estimation of vent-field scale fluxes from point-source measurements is not just the difficulty in locating and documenting all the different vent sources, but also the variability in the dimensions and geometry of the vent orifices themselves. While typical orifices are only a few centimeters across, some have been documented to be as large as 30 centimeters in diameter (e.g., Ginster et al., 1994).

Thus many studies have shifted their focus from the point-sources to the buoyant or neutrally-buoyant plumes above the vent fields, and thereby obtain a more naturally integrated estimate. Buoyant plumes from individual orifices may (or may not) merge as they rise vertically through the water column. Either way, the plumes entrain background fluid from near the vent structures and throughout their ascent (Turner, 1979; Bemis et al., 2002). Typically, plumes from high-temperature, focused hydrothermal sources rise a couple of hundred meters above the seafloor before reaching a height of neutral buoyancy, although the actual rise heights are determined by the buoyancy flux, background stratification, configuration of the source(s) and strength of the bottom water currents (Speer and Rona, 1989; Lavelle et al., 1998; Rona et al., 2002). After the plumes reach a height of neutral buoyancy, the fluid is advected away from the source area with the prevailing ocean currents at that depth (e.g. Rosenberg et al., 1988; Veirs et al., 1999; Lavelle et al., 2001; Thomson et al., 2003). We know that this fluid is broadly distributed through-

out the ocean basins, as chemical *signatures* of the high-temperature source fluid within these plumes are found 1000s of km from ridge axes (e.g., Lupton, 1998).

However, it is currently unclear to what degree the diffuse, lower-temperature flow near the sulfide edifices is entrained into these plumes. Preliminary field observations, which measured both the point sources and the buoyant plumes above hydrothermal structures, seemed to indicate that diffuse effluent near hydrothermal structures may not necessarily be entrained into the focused-vent source plume (Bemis et al., 1993; Ginster et al., 1994). This is significant since diffuse flow near vent structures can be substantial, and if it is entrained into the high-temperature plumes, then it is included in heat estimates obtained from water column surveys of neutrally-buoyant plumes. Diffuse percolation of hydrothermal fluids through or closely associated with hydrothermal structures may represent anywhere from one to five times the heat flux dissipated by the focused vent sources themselves (Schultz et al., 1992; Rona and Trivett, 1992; Baker et al., 1993; Lavelle and Wetzler, 1999; Lavelle et al., 2001). The effluent fluid velocities for this type of hydrothermal venting can also be substantial, with direct observations ranging from 0.005–0.15 m/s (Corliss et al., 1979; Rona and Trivett, 1992; Schultz et al., 1992, 1996; Schultz and Elderfield, 1997; Cooper et al., 2000).

The determining factors in the entrainment of background fluid near a vent structure may be the configuration of distributed high-temperature sources, and the mean speed of the bottom currents. Acoustic imaging of deep-sea hydrothermal plumes, as well as numerical simulations, show inward flow consolidation—a point of minimum radius—above distributed sources (Epstein and Burlach, 2001; Bemis et al., 2002; Rona et al., 2002; Jackson et al.,

2003). Thus they predict enhanced entrainment of fluid from the bottom boundary layer as the source area is expanded. There will also be a point of maximum vertical velocity associated with the 'neck' of the plume, below which the fluid is accelerating and above which it is decelerating (Fanneløp and Webber, 2003). However, given the substantial volume and heat flux predicted for diffuse percolation through sulfide structures, it is likely the buoyancy flux from this type of venting is significant enough to obtain a substantial rise height, even when not entrained into focused vent plumes. Estimating the partitioning of diffuse and focused flow fluid within neutrally buoyant plumes therefore requires detailed modeling and mapping of source configurations and flux rates, and would likely require additional constraints provided by chemical or biological tracers (e.g., Lavelle and Wetzler, 1999). Unfortunately, this leads us to conclude that an *a priori* estimate of the relative partitioning of distributed and focused vent fluids in the neutrally-buoyant plume is not feasible.

Lower-temperature, diffuse flow that is tens to hundreds of meters away from focused vent locals is well outside the defined source region of high-temperature vent structures, and thus this fluid is unlikely to be (initially) drawn into the high-temperature plumes (McDuff, 1994). Basalt-hosted, diffuse flow of this type generally has effluent temperatures which are less than 35 °C (Von Damm, 1995) and a single measurement from one of these vents showed exit velocities which were less than  $5 \times 10^{-5}$  m/s (Pruis and Johnson, 2004a). The buoyancy flux of these low-temperature diffuse vents is thus likely to be sufficiently small that their plumes will be blown over by bottom currents (which are of order 2–20 cm/s) and transported along the rock / water interface (Rona and Trivett, 1992; Trivett and Williams, 1994; Tivey et al., 2002).

Trivett (1994) developed a numerical model for low-temperature diffuse venting that predicts for a wide range of conditions (a) the rise height of these plumes will be less than their source dimension and (b) the plume may be transported a substantial distance while still maintaining contact with the rock / water interface. The eventual fate of this hydrothermal fluid remains uncertain, although studies have shown signatures of this fluid are still contained in the bottom mixed-layer several kilometers from their source regions (e.g., Trivett and Williams, 1994).

The present work describes a synthesis of heat flux data collected over three years along the Endeavour Segment of the Juan de Fuca ridge. The focus of this study is low-temperature, basalt-hosted diffuse vents away from high-temperature focused vents. Four separate vent fields are examined along a 2.5 km length of ridge axis (see Figure 1). Vertical heat flux measurements were obtained at  $\sim 0.5$  m height above the seafloor, both within and outside areas of active hydrothermal venting. In the next section, we describe the percolation of hydrothermal fluid through the upper basaltic crust and the fundamental aspects of heat transfer into the near-bottom oceanic boundary layer. Section 3 describes how the low-temperature fluid is mixed into the bottom boundary layer and sets the context for our observations near the rock / water interface. In section 4, a description of our turbulence instruments is given, including velocity calibration. The turbulence observations are then described in section 5. The time and space scales and the form and distribution of  $w'T'$  are shown for a range of heat flux magnitudes. These results show similar form for the different vent fields, most likely indicating the influence of similar geologic constraints on the advection of fluid (and thus heat) within the upper oceanic crust. Lastly, we compare statistical extrapolations of this result with previous

studies of hydrothermal heat flux in the ridge-axis environment.

## **2 Rock / Water Interface**

The thermal energy that drives the circulation of low-temperature fluids through the upper oceanic crust has the same source (i.e. the formation of the new seafloor) as the high-temperature systems, yet much less is known about its spatial, temporal and physical variability. The sub-surface flow-path, mixing history and geochemistry of diffuse effluent fluid has remained ambiguous. Low-temperature fluids near focused vent structures may be (1) conductively heated seawater, without large geochemical modification, (2) a mixture of high-temperature effluent with seawater or other reservoir fluid or (3) some combination of these two processes (James and Elderfield, 1996; Murton et al., 1999; Cooper et al., 2000; Butterfield et al., 2003). Secondary processes such as conductive heat loss (Cooper et al., 2000), mineral precipitation and / or dissolution (Tivey et al., 1995; James and Elderfield, 1996), re-equilibration of the vent fluids with the host rock at low temperature (Sedwick et al., 1992), or sub-seafloor biological processes (Johnson et al., 1988; Huber et al., 2002) may also affect the temperature–chemistry relationship of the hydrothermal fluid prior to discharging into the ocean. Given these ambiguities, substantial uncertainty remains in estimating the magnitude of mass and energy transport from low-temperature, diffusely venting regions of the seafloor. While one recent study by Murton et al. (1999) showed that more than 90% of the heat flux along one segment of the Mid-Atlantic Ridge is dissipated by conductively heated seawater or simple thermal conduction—with little or no geochemical modification—all studies which have examined geochemical data from ridge-

axis diffuse fluids as they discharge from the seafloor, support the involvement of a high-temperature source fluid (Butterfield et al., 2003).

Systematic, quantitative data on the prevalence and distribution of basalt-hosted, diffuse venting along spreading axes is currently lacking. However it is clear that considerable variability in the surface expression of venting of this type occurs between, and within, active vent sites. Most low-temperature, basalt-hosted venting occurs as small patches (a few meters in diameter) of flow that appears to be associated with local variability in the permeability of the rock structure—with the majority of flow occurring either along surface cracks or near regions of active faulting. However, much larger regions of venting do occur. The Clam Bed vent field (see Figure 1) is host to a large, 30 m × 50 m, area of diffuse venting. The region of active venting can clearly be delineated by the presence of an extensive tubeworm community. A small high-temperature, greater than 215 °C, vent is located near the center of this diffuse patch, but measurements of the temperature of the basalt-hosted flow are all still less than 30 °C.

Substantial variability in rock surface temperature does exist within the patch of diffuse venting however. In fact, measurements showed high variability even at decimeter scales. A collection of temperature measurements obtained using a 1-m triangular array of thermistors, which were kept in direct contact with the seafloor using spring-loaded pistons, showed variability of more than 10 °C over less than twenty centimeters (Figure 2 and Table 1), although there was no visual evidence in variability of the health of the tubeworms within the sampled areas (J. Voight, pers. comm., 2001). These observations demonstrate that at the rock / water interface, diffuse vents are more analogous to a collection of small micro-plumes emanating from discrete cracks than a large

distributed heat source. To better understand how these microplumes mix into the bottom boundary layer requires more information on the buoyancy of the hydrothermal fluid as it leaves the crust, and the rate at which the fluid is supplied to the interface. This is typically expressed as the surface buoyancy flux,

$$B_0 = b_0 w_0, \tag{1}$$

where  $b_0$  is the vertical buoyancy,  $b = -(g/\rho)\rho'$ , and  $g$  is the acceleration of gravity. Fluid density,  $\rho$ , is determined by the salinity, temperature and depth of venting. Generally, diffuse fluids have salinities near background seawater values (D. Butterfield, pers. comm., 2003), so for our calculations we have assumed the density contrast is due only to thermal effects. Thus we can write  $b = g\alpha\Delta T$ , where  $\alpha$  is the coefficient of thermal expansion and  $\Delta T$  is the temperature differential between the warm hydrothermal fluid and the cool background seawater. In point-source plume models, the total source buoyancy flux,  $\hat{B}_0$ , is the important factor, therefore the source volume flux,  $q = w_0 A$ , is used in equation (1) instead of the mean velocity of the venting fluid, where  $A$  is the cross-sectional area of the source.

The geology of the upper oceanic crust places important constraints on the volumetric fluid flow rate out of the basaltic crust, and thus has a large impact on the measured surface buoyancy flux. Similar to flow in the ocean, the vertical velocity of fluid within the porous media is controlled by the vertical buoyancy and the resistance to flow, in this case primarily the capacity of porous rock to transmit the fluid. Unfortunately, there is a large range in the measurements and estimates of the transport efficiency of the upper oceanic crust (see Fisher, 1998, for an overview). However, it is possible to

broadly constrain the velocity of the hydrothermal fluid as it flows through the crust. The one-dimensional volumetric flow rate per unit area,  $\bar{w}$ , which is driven by the vertical pressure gradient,  $dp/dz$ , due to the buoyancy of the hot hydrothermal water, can be expressed as

$$\bar{w} = -\frac{K}{\mu} \frac{dp}{dz} \approx -\frac{K\rho_0 b}{\mu}, \quad (2)$$

where  $K$  is the permeability of the host rock,  $\mu$  is the dynamic viscosity of the fluid and  $\rho_0$  is the density of the background seawater.

The vertical flow rate and temperature of the effluent fluid also directly determine the flux of heat through the seafloor interface, i.e.

$$Q = \rho c_p \bar{w} \Delta T, \quad (3)$$

where  $c_p$  is the specific heat capacity of the fluid. Comparing equations (2) and (3) demonstrates the interplay between geologic properties and the heat flux measured at the surface. In Figure 3, the specific discharge of fluid through the seafloor is plotted as a function of hydrothermal fluid temperature. It shows that for the range of heat flux estimates for diffuse hydrothermal flow, hundreds to tens of thousands of  $\text{W}/\text{m}^2$  (e.g., Rona and Trivett, 1992; Pruis and Johnson, 2004a), the specific discharge of fluid over the diffusely-venting region is between  $10^{-3}$  and  $10^{-6}$   $\text{m}/\text{s}$ , and that the effective permeability of the uppermost rock matrix must be between  $10^{-8}$  and  $10^{-11}$   $\text{m}^2$ .

If we are interested in estimating the effect of the individual micro-plumes emanating from the cracked surface of the basaltic basement rocks, then it is important to realize that the specific discharge calculated above is not the actual velocity of the fluid as it departs from the seafloor,  $w_0$ . The fluid in the

rock matrix is constrained to flow only within the open space of the porous media, so a geometric scaling is required to translate the specific discharge into the actual fluid velocity within the cracks in the substrate. Allowing for laminar flow, the scaling factor depends on the porosity of the media,  $\phi$ , and also the geometry of the fluid flow paths accessible for vertical flow. Simple permeability models yield scaling factors between  $1/\phi$  and  $3/\phi$ , although larger scaling factors are possible if the majority of the open pore space is unavailable for fluid flow (Bear, 1972). Ocean bottom gravity surveys have shown that the porosity of young uppermost oceanic crust ranges from 9–38% (see Pruis and Johnson, 2002, and references therein) and a recent gravity survey estimated that a mean porosity for the upper 130 meters of basaltic crust for the Endeavour Segment at the upper end of that range (Gilbert and Johnson, 1999). Thus while Figure 3 shows that if the advective heat fluxes from diffusely venting regions are of order 1000s  $\text{W}/\text{m}^2$ , the volumetric flow per unit area is of order  $10^{-5}$   $\text{m}/\text{s}$ ; using the above correction factors, this translates into interstitial pore fluid velocities which are as much as ten times larger, but are still  $\ll 1$   $\text{cm}/\text{s}$ . These calculations demonstrate that the vertical velocity of the effluent hydrothermal fluid from this type of venting is likely to be small in comparison to the typical horizontal velocities of bottom water, which are of order 2–20  $\text{cm}/\text{s}$ .

Before we cross the rock-water interface and examine the near-bottom turbulent boundary layer, it should be noted that the gradients in surface temperature shown in Figure 2 and Table 1 are unlikely to extend to substantial depth within the rock matrix. This is an important point since the heterogeneity seen at the surface is not likely to represent heterogeneity in the upwelling source fluid below the surface. The thermal capacity of the rock matrix would

quickly dissipate any excess thermal energy carried by the hydrothermal fluid. To demonstrate this point, we can estimate the surface heat flux between cracks within an otherwise uniform, un-broken block of basalt, using Fourier’s law of heat conduction. The heat flux through the basalt matrix can be written as

$$Q = -\Lambda \left( \frac{\partial T}{\partial y} \right)_{y=0}, \quad (4)$$

where  $\Lambda$  is the thermal conductivity of basalt,  $\sim 2.4 \text{ Wm}^{-2}\text{K}^{-1}$ , and  $T$  is the temperature of the rock matrix. Thus two cracks separated by 20 cm—one with its rock surface maintained by upwelling hydrothermal fluid at  $\leq 30 \text{ }^\circ\text{C}$ , and the other maintained at  $2 \text{ }^\circ\text{C}$ —would dissipate enough thermal energy to cool the volume of seawater in a 2-cm wide crack by an amount equivalent to the entire difference in fluid temperature in less than two hours. The actual rate of thermal dissipation in oceanic crust would likely be substantially greater. Even though the rock is likely to be fractured, and therefore have a lower effective thermal conductivity (Johnson and Pruis, 2003), the fluid flow paths within the rock are unlikely to be constrained to cracks as large as 2-cm. Thus the rock-water surface area, and consequently the interfacial heat transfer rate, is likely to be much larger than for the uniform block calculation above (Rohsenow et al., 1998; Lowell and Yao, 2002; Pruis and Johnson, 2004b). Therefore the observed gradients in rock surface temperature are likely due to variability in the surface permeability structure and near-surface mixing of the upwelling hydrothermal fluid with seawater, and not different reservoirs of upwelling hydrothermal fluid. These results imply that the uppermost basaltic rock likely represents the most heterogeneous region of temperature and fluid chemistry—since below the surface, large temperature gradients within the

upper basaltic crust cannot be maintained; and above the surface, mixing processes quickly homogenize any variability in fluid properties.

### 3 Diffuse hydrothermal plumes

Utilizing these results, we can examine the importance of the geometry and initial momentum of the individual micro-plumes in a cross-flow current. At distances  $x \gg L_M = (w_0 u)/b_0$ , the effect of the initial momentum of the plumes is negligible, and at  $L \gg r_0$ , where  $r_0$  is the radius of the source, initial geometry effects are negligible (Slawson and Csanady, 1967). Assuming a minimal salinity contribution and hydrothermal fluid temperatures between 3 and 40 °C,  $b_0$  would range between  $10^{-3}$  and  $10^{-1}$  m/s<sup>2</sup>. Using estimates for the bottom water velocity,  $u \sim 10^{-1}$  m/s, and the effluent fluid velocity,  $w_0 \sim 10^{-3}$  m/s, gives  $L_M < 10$  cm. Given that the individual sources are also constrained to small areas (see Figure 2 and Table 1), initial geometry effects of the micro-plumes are also fairly localized. Thus the geometry and initial momentum of the individual micro-plumes from low-temperature diffuse sources does not greatly impact the plume dynamics at measurement heights greater than several tens of centimeters.

While it is therefore more appropriate to discuss diffuse plume dynamics as originating from a distributed source area (similar to Maxworthy and Narmoussa, 1994), we will first look at the more well-studied point-source plumes, since the impact of a cross-flow current has been examined in more detail for point-sources, and also to facilitate comparisons with the high-temperature focused source plumes. Observational and laboratory studies for point-source plumes rising in a non-rotating, stratified environment with no cross-flow have

shown that the maximum rise height (e.g., Turner, 1979; Hanna et al., 1982; Lavelle, 1997) is

$$z_{max} \approx 3.75 \left( \frac{\hat{B}_0}{N^3} \right)^{1/4}, \quad (5)$$

where  $N$  is the buoyancy frequency,

$$N = \left( \frac{g}{\rho} \frac{d\rho}{dz} \right)^{1/2}. \quad (6)$$

Typical values of  $N$  are  $7.35 \times 10^{-4} \text{ s}^{-1}$  and  $1.68 \times 10^{-3} \text{ s}^{-1}$  for the depth range of 2100–2300 m in the Atlantic and Pacific oceans, respectively (Speer and Rona, 1989). Similarly, vertical CTD casts near our study area along the Endeavour Segment of the Juan de Fuca Ridge obtained by Veirs et al. (1999) yielded average values for  $N$  of  $2 \times 10^{-3} \text{ s}^{-1}$  and  $1.5 \times 10^{-3} \text{ s}^{-1}$  for observations above and within the near-bottom geothermal boundary layer, respectively. Our surveys in 2001 and 2002, utilizing a CTD mounted on the remotely-operated vehicle *Jason*, found  $N$  less than  $1 \times 10^{-3} \text{ s}^{-1}$  near the floor of the axial valley, generally between 1 and  $1.5 \times 10^{-3} \text{ s}^{-1}$  for the next 300 meters and approximately  $2 \times 10^{-3} \text{ s}^{-1}$  for observations above 400 meters above the seafloor (see Figure 4 for an example profile taken above the central valley instrument deployment site). A near-bottom low stability layer, which we define as the region below which the squared buoyancy frequency is less than a prescribed limit, in our case  $N^2 < 1 \times 10^{-6} \text{ s}^{-2}$ , was found to be generally  $< 35$  m in vertical dimension.

Salinity variation is an important contributor to the source buoyancy flux of high-temperature systems, where high-temperature hydrothermal fluid salinities range from 0.1 to 2 times that of seawater (Butterfield et al., 2003).

Given this complication and constrained by point source measurements at the seafloor, the range of source buoyancy fluxes used in numerical simulations is between  $0.1 \text{ m}^4/\text{s}^3$  for individual vent sources to  $2.1 \times 10^{-3} \text{ m}^4/\text{s}^3$  for distributed ( $100 \text{ m}^2$ ) sources (e.g., Speer and Rona, 1989; Lavelle, 1997). Using this entire range, one would expect rise heights anywhere between 80 and 375 m. However, the rise height of hydrothermal plumes is also sensitive to the cross-flow current (Hanna et al., 1982; Middleton, 1986; Lavelle, 1997) and from atmospheric observations it has been shown that

$$z_{max} \approx 2.6 \left( \frac{\hat{B}_0}{uN^2} \right)^{1/3}. \quad (7)$$

For a cross-flow velocity,  $u$ , of 0.2 m/s, and using the other values from above, the minimum of the estimated rise heights would decrease to approximately 60 meters above the seafloor.

Mixing depths for the distributed sources have primarily been studied from the perspective of generating deep and intermediate water sources at high latitudes. Numerical simulations and laboratory studies (Jones and Marshall, 1993; Maxworthy and Narimousa, 1994; Ivey et al., 1995; Visbeck et al., 1996) have shown that in a stratified ocean, the maximum depth (or in our case, height) of penetration is related to the radius,  $r_0$ , of the source region,

$$z_{max} \approx 3.9 \frac{(B_0 r_0)^{1/3}}{N}. \quad (8)$$

Given the large range possible for surface buoyancy fluxes and radii of diffusely venting patches of seafloor, rise heights anywhere up to  $\sim 75$  meters are reasonable. But for a typical diffuse patch of a few meters in diameter, a surface heat flux of a couple thousand  $\text{W}/\text{m}^2$ , and a buoyancy frequency of 1

$\times 10^{-3} \text{ s}^{-1}$ , the generated plume would reach a maximum height of 40 meters. However, cross-flow effects and an increase in the buoyancy frequency above the near-bottom low stability layer would likely decrease the maximum plume height somewhat. Thus typically, one would expect some vertical separation between the high-temperature and lower-temperature diffuse plumes as they advect away from their respective source regions. It should therefore be possible for water column surveys to differentiate between the two different source regimes, if surveys are extended to very near (perhaps, impractically near) the seafloor.

#### 4 Instrumentation and Data Collection

Vertical heat flux estimates were obtained at approximately 0.5 m height off bottom (hob). The on-bottom deployment intervals ranged from 5 hrs to 322 days (see Table 2). Shorter term deployments recorded continuously at 2 or 5 Hz, while year-long deployments were configured to record bursts of 180–320 samples at 2 Hz every hour. Each turbulence sensor package consisted of a central data logger which recorded synchronous measurements of temperature (3 point measurements within 0.8 m hob) and three-axis velocity (nominally at 0.51 m hob). The instruments were deployed with a novel single-point mooring design, which enabled stable instrument deployments in areas of rough volcanic-pillow basalt terrain (Figure 5). This deployment system eliminated the effects of current meter motion by having rigid contact of the mounting system with the seafloor, and also allowed for placement of the instrument package in the very rough surface morphology associated with most diffuse venting areas. The instrument packages were generally not placed closer than

10–15 meters from actively venting sulfide structures. The thermistors are encased in individual titanium pressure housings and have a measurement range of  $-5$  to  $+45$  °C. Thermistor precision is  $0.1$  °C and the resolution is  $0.03$  °C. The thermistors were calibrated prior to and following deployments utilizing a well-stirred ice bath which was slowly heated to  $40$  °C. The calibrations were verified by examining self-consistency within the thermistor chains during descent and ascent from the seafloor.

Acoustic velocity measurements were made using Nobska MAVS-3 (Thwaites and Williams, 1997). MAVS have previously been used in the deep sea deployments (Tivey et al., 2002; Veirs, 2003) because of their ability to measure small velocities with reasonably high accuracy ( $\sim 0.3$  cm/s). MAVS are differential time-of-flight velocity sensors and have a linear response function similar to the BASS instrument (Williams et al., 1987; Shaw and Trowbridge, 2001). This enables equal sensitivity at low velocities, but requires careful calibration to determine the zero-point. Each MAVS obtained zero-point measurements both prior and subsequent to the instruments deployment (for additional details on velocity calibrations see Williams, 2001). During the initial deployment of our instruments, large (up to  $4.5$  cm/s) offsets were noticed between the pre- and post-deployment calibrations. We have found that all of our MAVS-3 instruments exhibited offsets during their first full-ocean depth immersion in salt water. In all subsequent deployments, the zero-velocity calibrations varied by less than  $0.3$  cm/s from the initial post-deployment calibration values. We therefore believe that zero-offset drift for these instruments is small, and simply subtracted the post-deployment zero-point calibrations from all determinations of velocity.

The time-of-flight methodology for computing fluid velocities utilized by the

MAVS current meters involves acoustic receivers which are spaced at distances of approximately 10 cm. But due to the use of four separate acoustic paths, the instrument has an effective sample radius of only a couple of centimeters. Small corrections to the computed velocities are required for variation in the sampled fluid temperature, and thus the velocity measurements are not entirely independent of the temperature measurements. A thermistor was located along the instrument shaft just outside the acoustic velocity sensor array. Examination of the spectra from a typical MAVS deployment (e.g., Figure 6) shows that the maximum scale of turbulent motion occurs at length scales of roughly 0.45 meters, where the angular wavenumber,  $k = 2\pi f / \bar{u}$ , is a function of frequency,  $f$ , and the mean current speed,  $\bar{u}$ . The velocity sensor typically falls off almost three orders of magnitude before reaching its resolution limit of a few centimeters. The temperature sensor falls off much quicker due to its slow thermal time constant ( $\sim 5$  seconds), and thus has a lower resolution limit that is only capturing mixing lengths on the order of  $\leq 5$  cm. Still there is almost two orders of magnitude falloff from the dominant length scale, and we are therefore able to capture most of the variance that is responsible for the majority of the energy dissipation. The dominant turbulent motions can clearly be seen in the data records, which show periodic large variations on timescales of 30–60 seconds, corresponding to mixing lengths scales of 0.25–0.5 meters for a mean horizontal current of order 0.05 m/s (see Fig. 7 for some examples).

## 5 Turbulent Heat Flux

There is two limiting thermal convection regimes that are turbulence instruments at 0.51 m hob could be experiencing; (1) forced convection or (2) free convection. In free, or natural, convection, the movement of the fluid is due entirely to density gradients within the fluid, e.g. hot air rises over cold air. There is no external device or phenomenon which causes fluid motion. In forced convection, the fluid is forced to flow by an external factor—wind in the atmosphere, geostrophic or tidal currents in the ocean. Our measurements, which were generally obtained directly above areas venting warm hydrothermal fluid, but were quite close to the bottom boundary in a known cross-flow, will be experiencing some mixture of these two modes of convection. In a homogenous, neutrally stratified boundary layer, the Monin-Obukhov length is the ratio of production of turbulent kinetic energy due to the mechanical shear and the magnitude of buoyancy conversion, and defines the height above the surface where buoyant factors begin to dominate over shear production of turbulence from the horizontal flow. The generation of turbulent kinetic energy due to shear production can be expressed as

$$S = \tau \frac{\partial \bar{u}}{\partial z}, \quad (9)$$

where  $\tau = u_*^2$  is the kinematic Reynolds stress and  $u_* = (\langle u'w' \rangle^2 + \langle v'w' \rangle^2)^{1/4}$  is the local shear velocity. For our calculations, we used 17-minute averaging periods in determination of local shear velocity. Numerous observations of the time-averaged velocity gradient and the Reynolds stress have established that

$$\frac{\partial \bar{u}}{\partial z} = \frac{u_*}{\lambda}, \quad (10)$$

where  $\lambda$  is the length scale of the dominant turbulent motion (e.g., Prandtl, 1925). In a constant-stress, unstratified turbulent surface layer,  $\lambda = \kappa|z|$ , where  $\kappa$  is von Kármán's constant (taken to be 0.4) and  $z$  is the height above the surface. Using  $\lambda = \kappa|z|$ , the generation of turbulent kinetic energy due to shear production can be expressed as  $u_*^3/\kappa|z|$ .

The local rate of buoyancy conversion in the turbulent kinetic energy equation is

$$B = \langle w'b' \rangle = g\alpha \langle w'T' \rangle, \quad (11)$$

given that the buoyancy flux depends almost exclusively on the heat flux, i.e. the salinity flux is assumed negligible, for low-temperature diffuse vents. Thus we can estimate the Monin-Obukhov length from direct observations of  $u_*$  and  $\langle w'T' \rangle$ , or

$$L = -\frac{u_*^3}{\kappa g \alpha \langle w'T' \rangle} = -\frac{u_*^3 \rho_0 c_p}{\kappa g \alpha Q}. \quad (12)$$

Using the deployment average values given in Table 2, it can be shown the Monin-Obukhov length scale would be at all the deployment sites less than  $-1.5$  m ( $L$  is defined as negative for unstable conditions), although substantial variability exists on shorter timescales. At the 17-minute averaging timescale used for our calculations, it was not uncommon for both stable and unstable conditions to be sampled over the course of a multiday deployment, even near regions which exhibit rigorous venting.

The actual shape of the surface-layer velocity profile is influenced by the local state of stratification. Unstable conditions yield larger mixing length scales, while stable stratification yields dominant mixing scales which are smaller.

Most of our observations above diffuse vents are within a statistically unstable boundary layer, where the fluid density is generally lower near the seafloor interface than it is above. The Monin-Obukhov similarity theory has been extended though the use of stability functions which depend solely on  $z/L$  or

$$\frac{\partial \bar{u}}{\partial z} = \frac{u_*}{\kappa |z|} \Phi_m, \quad (13)$$

where the  $\Phi_m$  function were empirically determined to be

$$\Phi_m = \left(1 - 16 \frac{z}{L}\right)^{-1/4}, \quad (14)$$

and

$$\Phi_m = \left(1 + 5 \frac{z}{L}\right), \quad (15)$$

under unstable and stable conditions, respectively (Businger et al., 1971; Dyer, 1974). Thus a Monin-Obukhov length scale of  $-1.5$  meters would effectively increase the dominant mixing length from  $0.2$  to  $0.33$  m, although dominant mixing lengths of up to  $0.45$  m are not uncommon for shorter averaging timescales. Alternatively, it has been postulated that the mixing length may be proportional to the wavelength at the peak in the weighted vertical velocity spectrum, or  $\lambda_{peak} = c_\lambda/k_{max}$ , where  $c_\lambda = 0.85$  (McPhee and Martinson, 1994). Examples of the 1-hour average spectra are shown in Figure 8 and give reasonably good correspondence between the two methods, with  $\lambda_{peak}$  ranging from  $0.1$  to  $0.5$  m, but typically a value close to  $0.2$  to  $0.35$  m would be estimated.

The dissipation rate can also be calculated directly from the measured wave number velocity autospectra within the inertial subrange,

$$\varepsilon^{2/3} = \frac{3}{4\varphi} \Psi_{ww}(k) k^{5/3}, \quad (16)$$

where  $\Psi_{ww}$  is the vertical velocity energy density spectra at wavenumber  $k = 2\pi f/\bar{u}$  in the inertial subrange of the spectrum and  $\varphi$  is Kolmogorov's constant, taken to be 0.51 (Hinze, 1975; Gross and Nowell, 1985). In Figure 9, the deployment averaged mechanical shear production and the calculated buoyancy conversion are compared to the dissipation rate. The deployment averaged buoyancy conversion is everywhere less than half the estimated shear production, and the shear production is equal to or greater than the dissipation rate. From this comparison, it seems plausible that the overall importance of diffusely venting patches to the structure of turbulence in the near-bottom boundary layer lies in its enhancement of mechanical stirring, rather than in direct plume entrainment.

Turbulent heat fluxes were directly calculated from our measured vertical velocities and temperatures,

$$Q = \rho c_p \langle w'T' \rangle, \quad (17)$$

where  $\langle w'T' \rangle$  needs to be computed over timescales sufficiently long for statistical robustness, but sufficiently short to ensure the assumption of stationary. This time interval, chosen to be around 17 minutes, was easily obtained in our short-term deployments (which recorded continuously at either 2 or 5 Hz). But due to logistical constraints, the yearlong deployments only recorded bursts of measurements over a time interval of 90–160 seconds. These timescales are of

similar order to the scale of the dominant turbulent motions. To test whether we could obtain statistically reliable heat flux estimates utilizing only short, 1.5 to 2.5 minute, bursts of recordings, we compared the short-term, continuously recording deployments to results obtained from decimating these records to simulate the long-term sampling. The measured turbulent heat fluxes seem to indicate that the shorter sampling periods can underestimate the turbulent heat flux by as much as 50%, when short time averages are considered. But generally when averaged over multi-day deployments, the results were more comparable. We thus expect the turbulent heat fluxes estimated from the long-term deployments to be lower-bound estimates, but correct to order of magnitude.

## 6 Discussion

Comparison of the measured temperatures at the rock/water interface with the measured turbulent heat flux has shown that point measurements of surface interface temperature are a poor predictor of turbulent heat flux measured above the diffuse vent. This result is perhaps not completely surprising given the large spatial gradients in surface rock temperature shown in Figure 2 and Table 1. Nevertheless this result could also be a consequence of spatially variable permeability modifying the velocity of the effluent fluid, and thereby affecting the transport and discharge rate of hydrothermal fluid out of the seafloor, or surface roughness variability which may locally enhance or reduce the measured heat flux over the vent site. However, since our six year-long records did not show a strong correlation between the bottom thermistor and observed turbulent heat flux (examples are shown in Figure 10), it is most

plausible that the bottom thermistor measures only the temperature of very localized effluent fluid, and that this temperature may vary over small spatial distances. Even so, both the turbulent heat and the bottom thermistor temperatures did display variability on monthly to annual timescales. This variability may be indicative of slow variations in the permeability of the uppermost rock matrix due to mineral precipitation or dissolution or sub-seafloor biological productivity. However, without synchronous volume flux and fluid density measurements, it is impossible to distinguish between changes in the geologic properties of the sub-surface flow paths and the rate of heat supplied to the system (e.g., Pruis and Johnson, 2004a).

Several qualitative observations can be made from the turbulent heat flux observations we have obtained over basalt-hosted, diffusely venting patches of the seafloor. The probability and cumulative distribution functions for each of the vent fields studied are shown in Figure 11. The large skewness of the probability distribution indicates the efficiency with which heat is dispersed as the bigger eddies overturn. Similarly, the large kurtosis reinforces the view that most of the actual heat transfer takes place during intermittent events, and emphasizes the fact that there will be substantial variability in short-term averages of heat flux. The accuracy of such statistics depends strongly on the characteristics of the distributions, and if the tails of the distribution are poorly sampled, the mean values will likewise be poorly estimated. While the most common observed value of heat flux ranged from 50–730 W/m<sup>2</sup>, the mean values were an order of magnitude larger. Functionally, the Clam Bed vent field results are very similar to the observations of diffuse heat flux at the Main Endeavour vent field, although the mean heat flux was roughly half of that observed within the Main Endeavour Field. These two sites represent

the most comprehensively studied regions in our study. Clam Bed is mostly dominated by large areas of diffuse flow and has only three active sulfide structures. In contrast, Main Endeavour Field is dominated by large, focused-flow structures and has only small patches of basalt-hosted diffuse flow at any distance from the sulfide edifices. Yet for each vent field, only about 20% of the observations were above the calculated mean, and removal of the largest 5% of measured heat flux values reduces the mean by a factor of approximately one third. The consistency of the results most likely indicates some geologic control on the hydrothermal discharge, but human preferences for instrument placement on the seafloor cannot be totally excluded. Nonetheless, the range of turbulent heat fluxes observed and the measured temperatures of effluent hydrothermal fluid at the rock/water interface, indicate that diffuse flow may be preferentially located in regions of enhanced permeability, greater than  $10^{-10}$  m<sup>2</sup> from Figure 3 and Table 2.

A recent water column study of the Main Endeavour Field by Veirs (2003) has attempted to quantify the lateral transport of warm hydrothermal fluid within the axial valley, while also quantifying the flux of heat in the buoyant plumes above the vent field. Estimates of 50–150 MW were obtained for the lateral near-bottom transport (assumed to be related to low-temperature, diffusely venting sources) and  $650 \pm 150$  MW for the high-temperature buoyant sources (Veirs, 2003; Thomson et al., 2003). Extrapolation of our turbulence measurements, assuming the heat flux measured at 0.5 m is representative of the surface heat flux and that the region of diffusely venting seafloor is between 5–10%, yields  $700 \text{ m} \times 300 \text{ m} \times 0.05$  to  $0.10 \times 5500 \text{ W/m}^2$  or 60–115 MW, roughly consistent with the water column data. Similar scaling applied to the Clam Bed vent field, but using the smaller area of the vent field, a larger

percentage of seafloor having diffuse venting ( $\sim 25\%$ ), and a lower mean heat flux of  $1800 \text{ W/m}^2$  gives a similar range of heat flux between 30–75 MW. This result is of comparable magnitude to an earlier study of the focused heat flux from this vent field of  $122 \pm 61 \text{ MW}$  (Ginster et al., 1994).

## 7 Summary

The flux of mass and energy through the seafloor interface impacts the interactions of the biological, chemical and physical processes important to the development of deep-sea hydrothermal vent communities, and also the global ocean chemical balance (Murton et al., 1999; Lavelle and Wetzler, 1999; Marsh et al., 2001; van Dover et al., 2002; Thurnherr et al., 2002; Thomson et al., 2003; Mottl, 2003; Wheat et al., 2003). In this paper, we have examined the processes important for the advective transfer of heat from the basaltic upper oceanic crust to the near-bottom boundary layer via basalt-hosted, diffusely venting regions of a mid-ocean spreading ridge. Our observations indicate that the seafloor interface is very heterogeneous within these regions of diffuse venting. This variability at the interface is however quickly homogenized both above and below the surface. The turbulent heat transfer in the near-bottom surface layer ( $< 2 \text{ m}$  hob) is controlled by the mechanical production of shear due to bottom currents. However, substantial enhancement in the shear production was observed near sites exhibiting large surface heat fluxes. Plumes from the low-temperature diffuse sources are likely to be constrained within the bottom low-stability layer, and are not likely to be mixed into high-temperature neutrally-buoyant plume which is of order 100s of meters above the axial floor. While short-term observations of turbulent heat flux show large variability, a

mean heat flux between 2–5 kW/m<sup>2</sup> is probably reasonable for diffuse-patches in this study area. The measured heat fluxes imply permeabilities greater than 10<sup>-10</sup> m<sup>2</sup> for the uppermost basaltic crust.

## Acknowledgement

Special thanks to the National Deep Submergence Facility at WHOI, and particularly the ROV *Jason II* pilots and scientific watch standers, who performed the difficult task of deploying and recovering the instrumentation from the seafloor. C. Jones was co-PI of this experiment, and provided access to his insights and many stimulating discussions. B. Fredericks designed the instrument deployment housings. A. J. Williams III, A. T. Morrison and D. Schaaf of Nobska provided substantial assistance in overcoming several last-minute engineering challenges. Research was funded by NSF grants OCE9911523 and OCE0085615.

## References

- Baker, E. T., G. J. Massoth, S. L. Walker and R. W. Embley, 1993. A method for quantitatively estimating diffuse and discrete hydrothermal discharge, *Earth and Planetary Science Letters* 118, 235–249.
- Bear, 1972. *Dynamics of Fluids in Porous Media*, Elsevier, New York, 764 pp.
- Bemis, K. G., R. P. Von Herzen and M. J. Mottl, 1993. Geothermal heat flux from hydrothermal plumes on the Juan de Fuca Ridge, *Journal of Geophysical Research* 98, 6351–6365.

- Bemis, K. G., P. A. Rona, D. Jackson, C. Jones, D. Silver and K. Mitsuzawa, 2002. A comparison of black smoker hydrothermal plume behavior at Monolith Vent and at Clam Acres Vent Field: Dependence on source configuration, *Marine Geophysical Researches* 23, 81–96.
- Businger, J. A., J. C. Wyngaard, Y. Izumi and E. F. Bradley, 1971. Flux-profile relationships in the atmospheric surface layer, *Journal of the Atmospheric Sciences* 28, 181–189.
- Butterfield, D. A., R. E. McDuff, M. J. Mottl, M. D. Lilley, J. E. Lupton and G. J. Massoth, 1994. Gradients in the composition of hydrothermal fluids from the Endeavour Segment vent field: Phase separation and brine loss, *Journal of Geophysical Research* 99 (B5), 9561–9583.
- Butterfield, D. A., W. E. Seyfried Jr. and M. D. Lilley, 2003. Composition and evolution of hydrothermal fluids, In: P. E. Halback, V. Tunnicliffe and J. R. Hein (Eds.), *Energy and Mass Transfer in Marine Hydrothermal Systems*, Dahlem University Press, Berlin, 123–162.
- Cooper, M. J., H. Elderfield and A. Schultz, 2000. Diffuse hydrothermal fluids from Lucky Strike hydrothermal vent field: Evidence for a shallow conductively heated system, *Journal of Geophysical Research* 105 (B8), 19269–19375.
- Corliss, J. B., J. Dymond, L. I. Gordon, J. M. Edmond, R. P. Von Herzen, R. D. Ballard, K. Green, D. Williams, A. Brainbridge, K. Crane and T. H. Van Andel, 1979. Submarine thermal springs on the Galapagos Rift, *Science* 203, 1073–1083.
- Delaney, J. R., V. Robigou, R. E. McDuff and M. K. Tivey, 1992. Geology of a vigorous hydrothermal system on the Endeavour Segment, Juan de Fuca Ridge, *Journal of Geophysical Research* 97, 19663–19682.
- Dyer, A. J., 1974. A review of flux-profile relationships, *Boundary-Layer Me-*

- teorology* 7, 363–372.
- Epstein, M. and J. P. Burlach, 2001. Vertical mixing above a steady circular source of buoyancy, *International Journal of Heat and Mass Transfer* 44, 526–536.
- Fanneløp, T. K. and D. M. Webber, 2003. On buoyant plumes rising from area sources in a calm environment, *Journal of Fluid Mechanics* 497, 319–334.
- Fisher, A. T., 1998. Permeability within basaltic oceanic crust, *Reviews of Geophysics* 26 (2), 143–182.
- Gilbert, L. A. and H. P. Johnson, 1999. Direct measurements of oceanic crustal density at the northern Juan de Fuca Ridge, *Geophysical Research Letters* 26 (24), 3633–3636.
- Ginster, U., M. J. Mottl and R. P. Von Herzen, 1994. Heat flux from black smokers on the Endeavour and Cleft Segments, Juan de Fuca Ridge, *Journal of Geophysical Research* 99 (B3), 4937–4950.
- Gross, T. F. and A. R. M. Nowell, 1985. Spectral scaling in a tidal boundary layer, *Journal of Physical Oceanography* 15 (5), 496–508.
- Hanna, S. R., G. A. Briggs and R. P. Hosker Jr., 1982. *Handbook of Atmospheric Diffusion*, Tech. Inf. Cent., U. S. Dept. of Energy, Washington D.C., 102 pp.
- Hinze, J. O., 1975. *Turbulence*, McGraw-Hill, New York, 790 pp.
- Huber, J., D. A. Butterfield and J. Baross, 2002. Temporal changes in archaeal diversity and chemistry in a mid-ocean ridge seafloor habitat, *Applied Environmental Microbiology* 68, 1585–1594.
- Ivey, G., J. Taylor and M. Coates, 1995. Convectively driven mixed layer growth in a rotating, stratified fluid, *Deep-Sea Research* 95, 331–349.
- Jackson, D. R., C. D. Jones, P. A. Rona and K. G. Bemis, 2003. A method for Doppler acoustic measurement of black smoker flow fields, *Geochemistry*,

- Geophysics, Geosystems* 4 (11), 1095, doi:10.1029/2003GC000509.
- James, R. H. and H. Elderfield, 1996. Chemistry of ore forming fluids and mineral formation rates in an active hydrothermal sulfide deposit on the Mid-Atlantic Ridge, *Geology* 24, 1147–1150.
- Johnson, K. S., J. J. Childress, R. R. Hessler, C. M. Sakamoto-Arnold and C. L. Beehler, 1988. Chemical and biological interactions in the Rose Garden hydrothermal vent field, Galápagos spreading center, *Deep-Sea Research* 35, 1723–1744.
- Johnson, H. P., and 17 others, 2002. Survey studies hydrothermal circulation on the Northern Juan de Fuca Ridge, *Eos, Transactions, American Geophysical Union*, 83 (8), 73, 78–79.
- Johnson, H. P., and M. J. Pruis, 2003. Fluxes of fluid and heat from the oceanic crustal reservoir, *Earth and Planetary Science Letters*, 216, 565–574.
- Jones, H. and J. Marshall, 1993. Convection with rotation in a neutral ocean: A study of open-ocean deep convection, *Journal of Physical Oceanography*, 23, 1009–1039.
- Lavelle, J. W., 1997. Buoyancy-driven plumes in rotating, stratified cross flows: plume dependence on rotation, turbulent mixing, and cross-flow strength, *Journal of Geophysical Research* 102 (C2), 3405–3420.
- Lavelle, J. W., E. T. Baker and G. J. Massoth, 1998. On the calculation of total heat, salt and tracer fluxes from ocean hydrothermal events, *Deep-Sea Research II* 45, 2619–2636.
- Lavelle, J. W. and M. A. Wetzler, 1999. Diffuse venting and background contributions to chemical anomalies in a neutrally buoyant ocean hydrothermal plume, *Journal of Geophysical Research* 104 (C2), 3201–3209.
- Lavelle, J. W., M. A. Wetzler and R. W. Embley, 2001. Prospecting for hydrothermal vents using moored current and temperature data: Axial Vol-

- cano on the Juan de Fuca Ridge, Northeast Pacific, *Journal of Physical Oceanography* 31, 827–838.
- Little, S. A., K. D. Stolzenbach and R. P. Von Herzen, 1987. Measurements of plume flow from a hydrothermal vent field, *Journal of Geophysical Research* 92 (B3), 2587–2596.
- Lowell, R. P. and Y. Yao, 2002. Anhydrite precipitation and the extent of hydrothermal recharge zones at ocean ridge crests, *Journal of Geophysical Research* 107 (B9), 2183, 10.1029/2001JB001289.
- Lupton, J., 1998. Hydrothermal helium plumes in the Pacific Ocean, *Journal of Geophysical Research* 103 (C8), 15853–15868.
- Marsh, A. G., L. S. Mullineaux, C. M. Young and D. T. Manahan, 2001. Larval dispersal potential of the tubeworm *Riftia pachyptila* at deep-sea hydrothermal vents, *Nature* 411, 77–80.
- Maxworthy, T. and S. Narimousa, 1994. Unsteady, turbulent convection into a homogeneous, rotating fluid, with oceanographic applications, *Journal of Physical Oceanography* 24 (5), 865–887.
- McDuff, R. E., 1994. Physical dynamics of deep-sea hydrothermal plumes, In: *Seafloor hydrothermal systems: Physical, chemical, biological, and geological interactions*, Geophysical Monograph Series 91, 317–346.
- McPhee, M. G. and D. G. Martinson, 1994. Turbulent mixing under drifting pack ice in the Weddell Sea, *Science* 263, 218–221.
- Middleton, J. H., 1986. The rise of forced plumes in a stably stratified cross-flow, *Boundary-Layer Meteorology* 36, 187–199.
- Mottl, M. J., 2003. Partitioning of energy and mass fluxes between mid-ocean ridge axes and flanks at high and low temperature, In: P. E. Halback, V. Tunnicliffe and J. R. Hein (Eds.), *Energy and Mass Transfer in Marine Hydrothermal Systems*, Dahlem University Press, Berlin, pp. 271–286.

- Murton, B. J., L. J. Redbourn, C. R. German and E. T. Baker, 1999. Sources and fluxes of hydrothermal heat, chemicals and biology within a segment of the Mid-Atlantic Ridge, *Earth and Planetary Science Letters* 171, 301–317.
- Pruis, M. J. and H. P. Johnson, 2002. Age dependent porosity of young upper oceanic crust: Insights from seafloor gravity studies of recent volcanic eruptions, *Geophysical Research Letters* 29 (5), 10.1029/2001GL013977.
- Prandtl, L., 1925. Bericht über Untersuchungen zur ausgebildeten Turbulenz, *Zeitschrift für angewandte Mathematik und Mechanik* 5 (2), 136–139.
- Pruis, M. J. and H. P. Johnson, 2004a. Tapping into the sub-seafloor: examining diffuse flow and temperature from an active seamount on the Juan de Fuca Ridge, *Earth Planetary Science Letters* 271 (3–4), 379–388.
- Pruis, M. J. and H. P. Johnson, 2004b. Tidal modulation of hydrothermal effluent temperature, *Journal of Geophysical Research* submitted.
- Rohsenow, W. M., J. P. Hartnett and Y. I. Cho, 1998. *Handbook of heat transfer*, New York, McGraw-Hill, 1483 pp.
- Rona, P. A. and D. A. Trivett, 1992. Discrete and diffuse heat transfer at ASHES vent field Axial Volcano, Juan de Fuca Ridge, *Earth Planetary Science Letters* 109, 57–71.
- Rona, P. A. K. G. Bemis, D. Silver and C. D. Jones, 2002. Acoustic imaging, visualization, and quantification of buoyant hydrothermal plumes in the ocean, *Marine Geophysical Researches* 23, 147–168.
- Rosenberg, N. D., J. E. Lupton, D. Kadko, R. Collier, M. D. Lilley and H. Pak, 1988. Estimation of heat and chemical fluxes from a seafloor hydrothermal vent field using radon measurements, *Nature* 334, 604–607.
- Robigou, V., J. R. Delaney and D. S. Stakes, 1993. Large massive sulfide deposits in a newly discovered active hydrothermal system, the High-Rise Field, Endeavour Segment, Juan de Fuca Ridge, *Geophysical Research Let-*

- ters 20 (17), 1887–1890.
- Schultz, A., J. R. Delaney and R. E. McDuff, 1992. On the partitioning of heat flux between diffuse and point source seafloor venting, *Journal of Geophysical Research* 97, 12299–12314.
- Schultz, A., P. Dickson and H. Elderfield, 1996. Temporal variations in diffuse hydrothermal flow at TAG, *Geophysical Research Letters* 23, 3471–3474.
- Schultz, A. and H. Elderfield, 1997. Controls on the physics and chemistry of seafloor hydrothermal circulation, *Philosophical Transactions: Mathematical, Physical and Engineering Sciences* 305 (1723), 387–425.
- Sedwick, P. N., G. M. McMurtry and J. D. Macdougall, 1992. Chemistry of hydrothermal solutions from Peles Vents, Loihi Seamount, Hawaii, *Geochimica et Cosmochimica Acta* 56, 3643–3667.
- Shaw, W. J. and J. H. Trowbridge, 2001. The direct estimation of near-bottom turbulent fluxes in the presence of energetic wave motions, *Journal of Atmospheric and Oceanic Technology* 18, 1540–1557.
- Slawson and Csanady, 1967. On the mean path of buoyant, bent-over chimney plumes, *Journal of Fluid Mechanics* 28, 311–322.
- Speer, K. G. and P. A. Rona, 1989. A model of an Atlantic and Pacific hydrothermal plume, *Journal of Geophysical Research* 94 (C5), 6213–6220.
- Thomson, R. E., S. F. Mihály, A. B. Rabinovich, R. E. McDuff, S. R. Veirs, and F. R. Stahr, 2003. Constrained circulation at Endeavour ridge facilitates colonization by vent larvae, *Nature* 424, 545–549.
- Thurnherr, A. M., K. J. Richards, C. R. German, G. F. Lane-Serff and K. G. Speer, 2002. Flow and mixing in the rift valley of the Mid-Atlantic Ridge, *Journal of Physical Oceanography* 32, 1763–1778.
- Thwaites, F. T. and A. J. Williams III, 1997. New current meter development, *Sea Technology* 4, 108–112.

- Tivey, M. K., S. E. Humphris, G. Thompson, M. D. Hannington and P. A. Rona, 1995. Deducing patterns of fluid flow and mixing within the TAG active hydrothermal mound using mineralogical and geochemical data, *Journal of Geophysical Research* 100, 12527–12555.
- Tivey, M. K., A. M. Bradley, T. M. Joyce and D. Kadko, 2002. Insights into tide-related variability at seafloor hydrothermal vents from time-series temperature measurements, *Earth and Planetary Science Letters* 202, 693–707.
- Trivett, D. A., 1994. Effluent from diffuse hydrothermal venting 1. A simple model of plumes from diffuse hydrothermal sources, *Journal of Geophysical Research* 99 (C9), 18403–18415.
- Trivett, D. A. and A. J. Williams III, 1994. Effluent from diffuse hydrothermal venting 2. Measurement of plumes from diffuse hydrothermal vents at the southern Juan de Fuca Ridge, *Journal of Geophysical Research* 99 (C9), 18417–18432.
- Turner, J. S., 1979. *Buoyancy effects in fluids*, B. K. Batchelor and J. W. Miles (Eds.), Cambridge University Press, Cambridge, 368 pp.
- Von Damm, K. L., 1995. Controls on the chemistry and temporal variability of seafloor hydrothermal fluids, In: *Seafloor Hydrothermal Systems: Physical, Chemical, Biological, and Geological Interactions*, Geophysical Monograph Series 91, American Geophysical Union, 222–246.
- van Dover, C. L., C. R. German, K. G. Speer, I. M. Parson and R. C. Vrijenhoek, 2002. Evolution and biogeography of deep-sea vent and seep invertebrates, *Science* 295, 1253–1257.
- Veirs, S. R., R. E. McDuff, M. D. Lilley and J. R. Delaney, 1999. Locating hydrothermal vents by detecting buoyant, advected plumes, *Journal of Geophysical Research* 104 (B12), 29239–29247.
- Veirs, S. R., 2003. Heat flux and hydrography at a submarine volcano: Ob-

- servations and models of the Main Endeavour vent field in the Northeast Pacific, PhD thesis, University of Washington.
- Visbeck, M., J. Marshall and H. Jones, 1996. Dynamics of isolated convective regions in the ocean, *Journal of Physical Oceanography* 26, 1721–1734.
- Wheat, C. G., J. McManus, M. J. Mottl and E. Giambalvo, 2003. Oceanic phosphorus imbalance: Magnitude of the mid-ocean ridge flank hydrothermal sink, *Geophysical Research Letters* 30 (17), 1895, 10.1029/2003GL017218.
- Williams, A. J. III, J. S. Tocho, R. L. Koehler, W. D. Grant, T. F. Gross and C. V. R. Dunn, 1987. Measurement of turbulence in the oceanic bottom boundary layer with an acoustic current meter array, *Journal of Atmospheric and Oceanic Technology* 4, 312–327.
- Williams, A. J. III, 2001. Acoustic current meter zero offset drift, *Oceans 2001*, 916–921.

Table 1

Mean temperatures over deployment interval for twelve contact thermistors deployed within a tubeworm vent field. Thermistor accuracy was 0.002 °C, although only 0.1 °C is shown for clarity. Deployment times are given with day in the month of June, 2001, followed by the time in UTM.

Thermistor <sup>†</sup>	Dep. 1	Dep. 2	Dep. 3	Dep. 4	Dep. 5
A	2.2	—	—	—	—
B	>18	2.2	5.8	7.0	—
C	2.2	2.2	2.9	2.0	—
D	—	—	—	—	—
E	>18	2.8	2.0	7.9	6.7
F	7.5	5.8	2.3	2.0	3.4
G	4.9	3.8	2.9	2.0	7.1
H	3.0	2.7	2.3	2.5	6.7
J	4.3	2.2	2.3	2.0	5.7
K	2.1	1.9	1.9	2.0	2.2
L	7.8	>18	2.0	2.5	2.4
M	6.6	5.9	2.0	2.1	6.2
$t_{\text{deployed}}$	19 14:00	19 16:50	19 19:50	22 04:30	24 23:40
$t_{\text{recovered}}$	19 16:40	19 19:38	22 04:23	24 23:10	25 04:12

<sup>†</sup>See Fig. 2 for thermistor locations.

Table 2

Deployment interval averages and ninety-five percent confidence intervals determined using the bootstrap method. Dissipation rate was estimated from the spectra by means of equation (16), other quantities were calculated directly from observations of velocity and temperature. Time intervals where frozen turbulence test failed were excluded from all averages shown.

Year	$\Delta t$ (days)	Location	$\bar{u}$ (m/s)	$\overline{\rho c_p \langle w' T' \rangle}$ (W/m <sup>2</sup> )	$\bar{u}_*$ (m/s)	$\bar{\epsilon} \times 10^{-6}$ (W/kg)
2002	2.0	MEF <sup>†</sup>	0.038	4700 ± 660	0.014	6.81 ± 1.63
2002	3.0	Mid. Valley <sup>††</sup>	0.029	10 ± 2	0.005	0.22 ± 0.04
2002	1.5	MEF <sup>††</sup>	0.033	12000 ± 1400	0.014	5.17 ± 1.16
2001	4.0	Clam Bed	0.032	100 ± 590	0.012	6.18 ± 0.69
2001	2.5	High Rise	0.096	110 ± 75	0.011	4.89 ± 1.16
2001	1.7	MEF	0.065	38000 ± 6000	0.030	80.7 ± 11.6
2001	6.2	MEF	0.045	150000 ± 6600	0.038	232. ± 30.6
2001	5.8	Clam Bed	0.037	35000 ± 1800	0.020	17.8 ± 1.54
2001	2.5	High Rise	0.059	4 ± 6	0.008	3.08 ± 0.60
2001	5.3	MEF	0.020	9800 ± 1100	0.017	11.0 ± 2.58
2001	5.8	Raven	0.048	35000 ± 2200	0.020	21.6 ± 1.69
2001	5.8	Raven	0.027	3700 ± 270	0.014	10.8 ± 0.82
2000	3.0	MEF	0.028	620 ± 170	0.009	2.74 ± 0.52
2000	0.2	Clam Bed	0.033	750 ± 230	0.011	3.97 ± 1.57
2000	3.2	MEF	0.042	26 ± 23	0.009	3.40 ± 0.74
2000	3.2	MEF	0.033	3000 ± 580	0.015	9.34 ± 1.34
2000	2.9	MEF	0.032	710 ± 120	0.010	3.56 ± 0.50
2000	0.5	Clam Bed	0.041	13 ± 14	0.007	0.74 ± 0.40
2000	6.0	MEF	0.041	19000 ± 1400	0.022	46.5 ± 7.13
2000/1	251.2	MEF <sup>‡</sup>	0.025	2100 ± 160	0.013	19.7 ± 1.37
2000/1	253.6	Clam Bed <sup>‡</sup>	0.029	460 ± 54	0.007	5.09 ± 0.41
2000/1	256.6	Clam Bed <sup>‡</sup>	0.026	970 ± 40	0.010	7.06 ± 0.46
2001/2	242.7	MEF	0.032	1100 ± 72	0.011	6.41 ± 0.51
2001/2	291.0	Raven	0.039	2200 ± 180	0.011	8.32 ± 0.37
2001/2	321.7	MEF	0.046	2600 ± 120	0.011	8.33 ± 0.46

<sup>†</sup>See Figures 6, 7, and 8.

<sup>††</sup>See Figures 7 and 8.

<sup>‡</sup>See Figure 10.

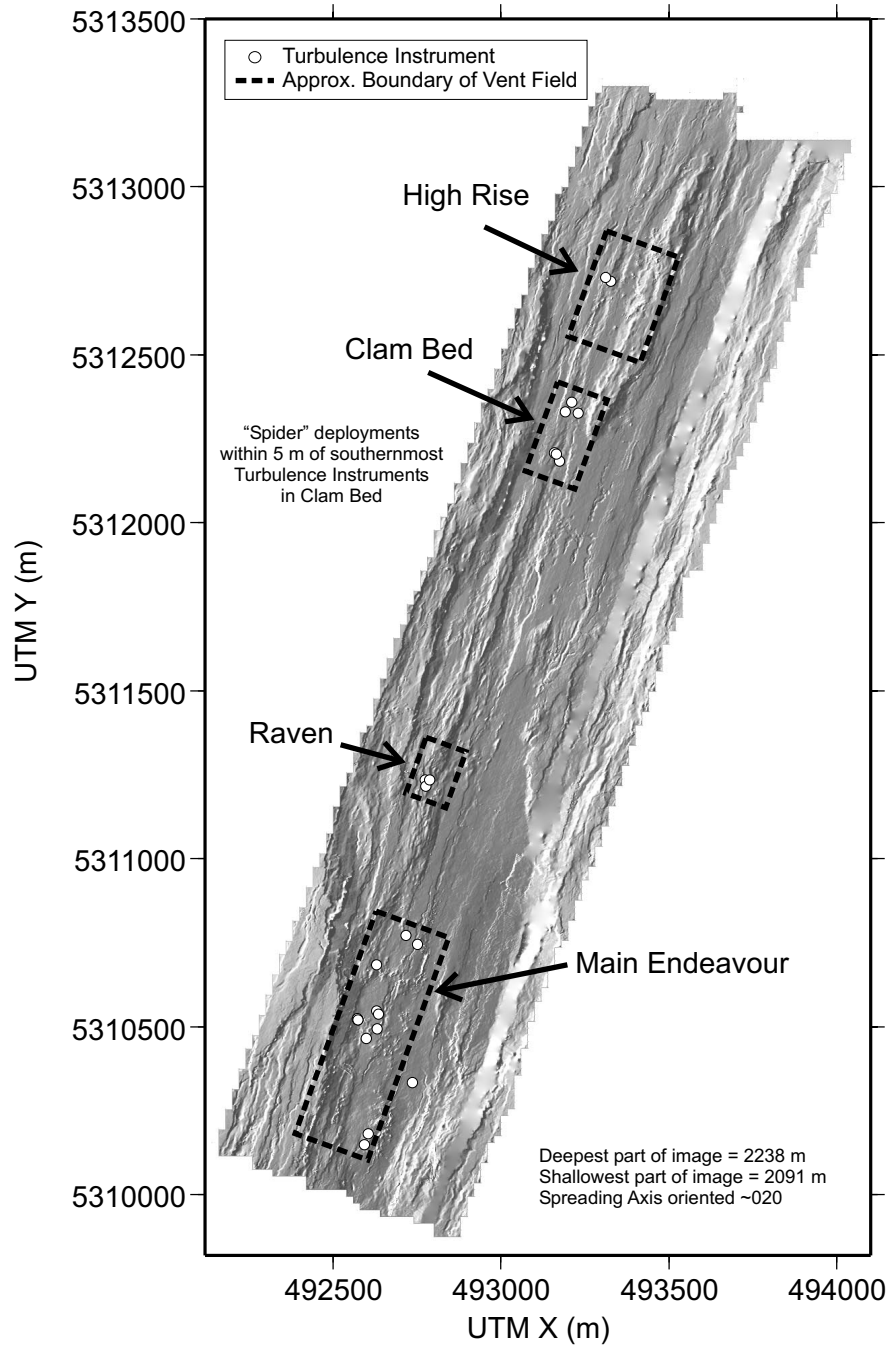


Fig. 1. Location map of the Endeavour Segment on the Juan de Fuca Ridge. High Rise and Main Endeavour fields are the most active of the four vent sites shown. Each has over 10 large sulfide structures displaying vigorous venting. In contrast, the Raven and Clam Bed fields exhibit relatively large areas of low-temperature, basalt-hosted diffuse flow, yet each contains three or less structures exhibiting focused venting. The shown bathymetry is from a high-resolution survey collected in 2000 and 2001 (Johnson et al., 2002).

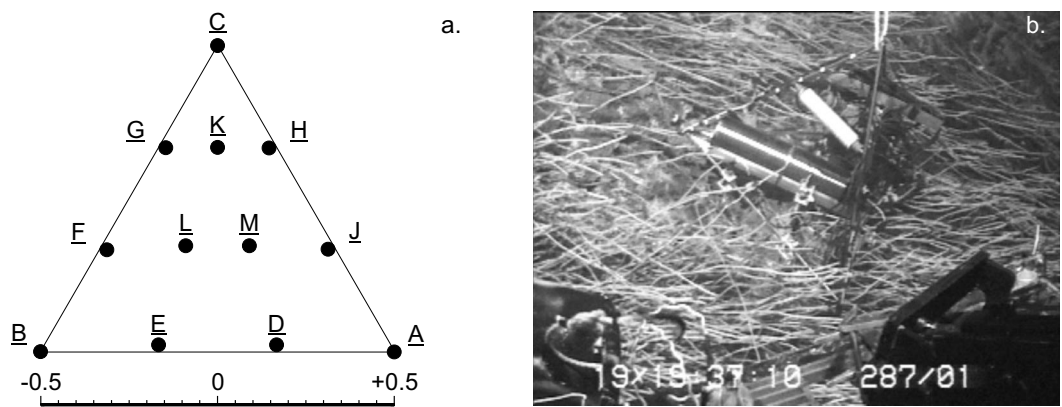


Fig. 2. (a) The "spider" instrument was designed to examine the spatial variability of surface temperature at the rock / water interface on the scale of decimeters. Twelve high-resolution thermistors were deployed over less than 1 m<sup>2</sup> of seafloor with spring-loaded contact plungers (see Table 1 for data). (b) The five deployments were all within a large tubeworm field in the Clam Bed vent field.

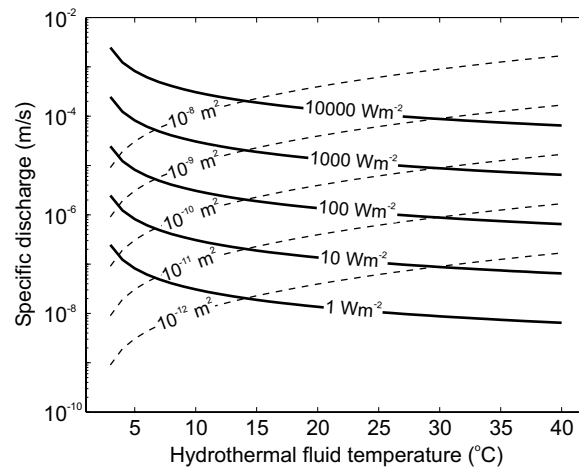


Fig. 3. Volumetric flow per unit area of seafloor,  $\bar{w}$ , for different hydrothermal fluid temperatures at different crustal permeabilities (dashed-lines) or heat fluxes (solid-lines). Pressure gradient within the crust is assumed hydrostatic and all the buoyancy is thermally-derived, i.e. the salinity of the hydrothermal fluid is assumed equal to seawater.

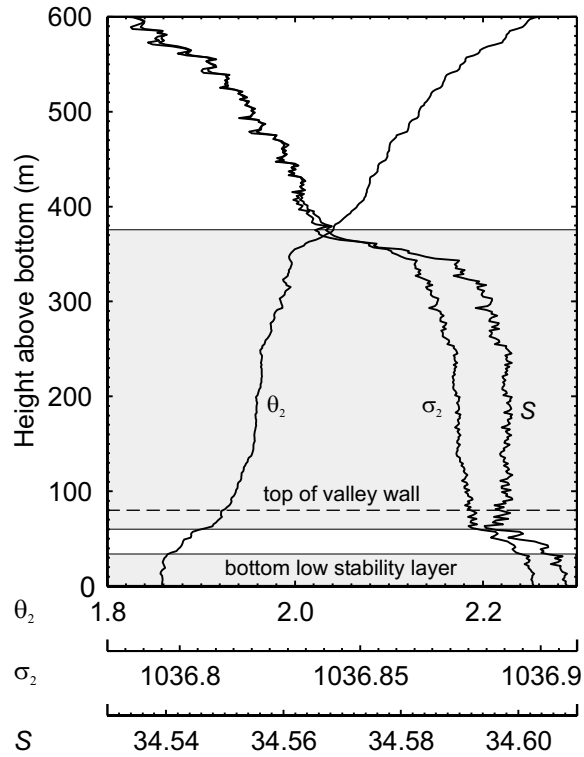


Fig. 4. Potential temperature ( $\theta_2$ ), potential density ( $\sigma_2$ ), and salinity ( $S$ ) profile above the central valley deployment (see Figure 1). A bottom low stability layer and range of rise heights predicted for high-temperature focused vent sources are shaded. The depth of the top of the axial valley wall is shown with a dashed line.

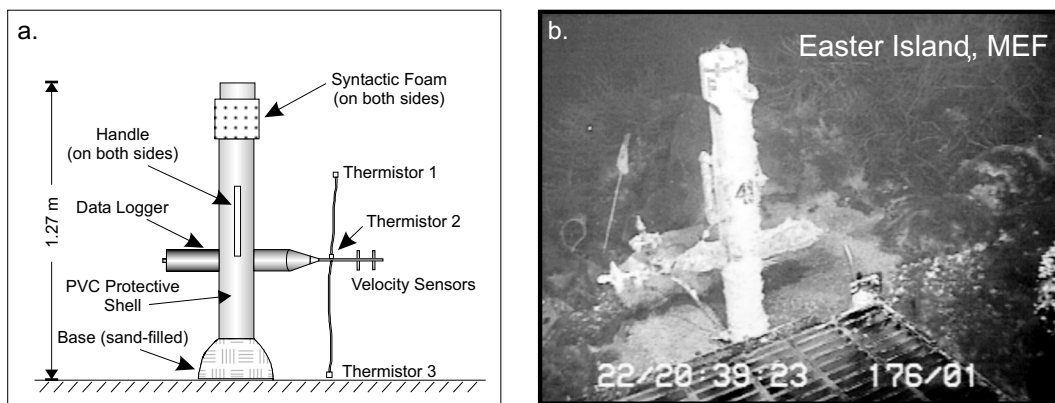


Fig. 5. (a) Schematic of the single-point mounting system which was utilized for deployment of the turbulence sensors on the seafloor. The instrument retracted into the PVC housing when carried along the seafloor by the remotely operated vehicle. (b) Image of instrumentation during recovery after a one-year long deployment. Biological coating of the instruments was common during long-term deployments.

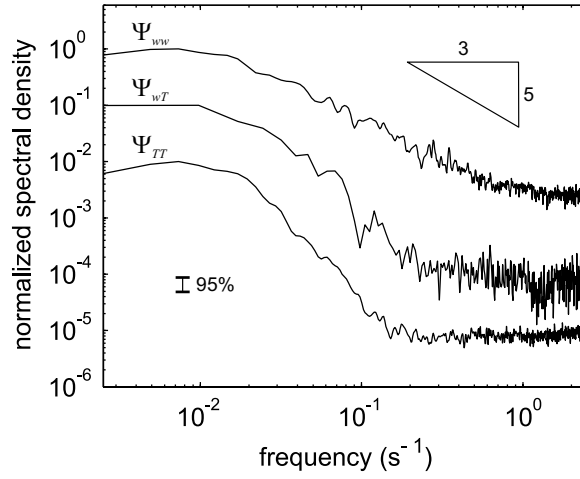


Fig. 6. Normalized power spectra for one-hour time series of  $w'$ ,  $w'T'$  and  $T'$ , covering the time period shown in Figure 7a. The  $w'T'$  and  $T'T'$  spectra were offset one decade downward for clarity. The approximate 5-second thermal time constant for the thermistors is evident, but most energy is at larger wavelengths. Total variances are  $\langle w'w' \rangle = 1.70 \times 10^{-4} \text{ m}^2 \text{ s}^{-2}$ ,  $\langle w'T' \rangle = 1.94 \times 10^{-4} \text{ m s}^{-1} \text{ K}$  and  $\langle T'T' \rangle = 6.20 \times 10^{-3} \text{ K}^2$ . The mean current speed,  $\bar{u}$ , is 0.038 m/s.

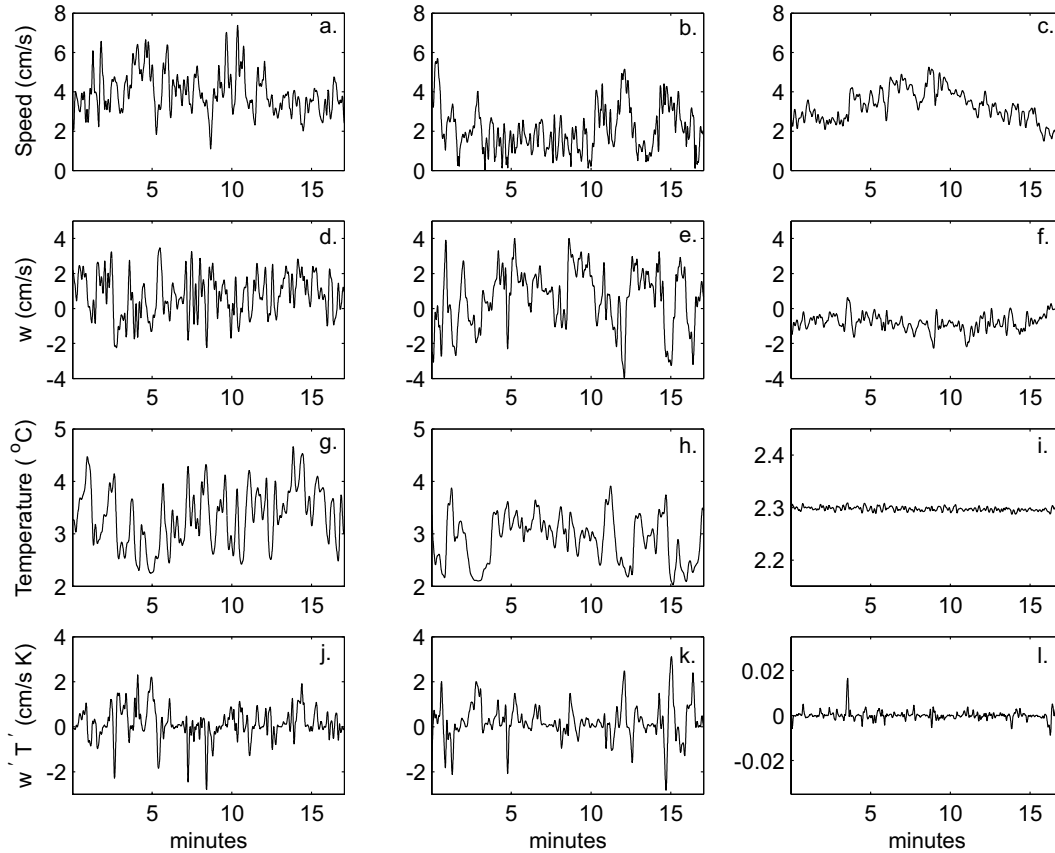


Fig. 7. Samples of typical 17-min records. Columns 1 and 2 contain data from two MAVS placed approximately 4 meters apart during the 2002 field program in the Easter Island area within the Main Endeavour Field. Column 3 is from a MAVS placed in the central valley, approximately 250 meters east of this site during the same time interval. Most of the energy is at temporal scales of less than one minute [see (a)-(f)]. Mean turbulent heat fluxes over this interval are 5900, 8900 and 2  $\text{W/m}^2$  for (j), (k) and (l), respectively. Note the change of one and two orders of magnitude in the scales of panels (i) and (l) respectively.

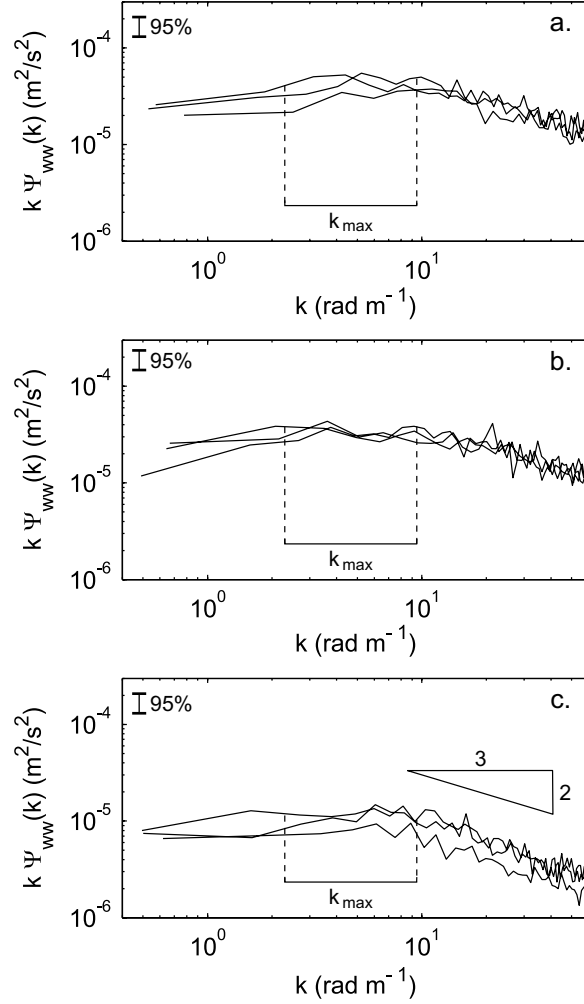


Fig. 8. Examples of smoothed 1-hour spectra, corresponding to the instruments shown in Figure 7a, b, and c, plotted versus the wave number,  $k = 2\pi f/\bar{u}$ , where  $\bar{u}$  ranges from 2.8 to 4.4 cm/s for the deployment intervals shown above. Dashed lines mark the spectral peak,  $k_{max} = c_\lambda/\lambda_{peak}$ . Dissipation rate may be estimated at any point within the  $-2/3$  slope region.

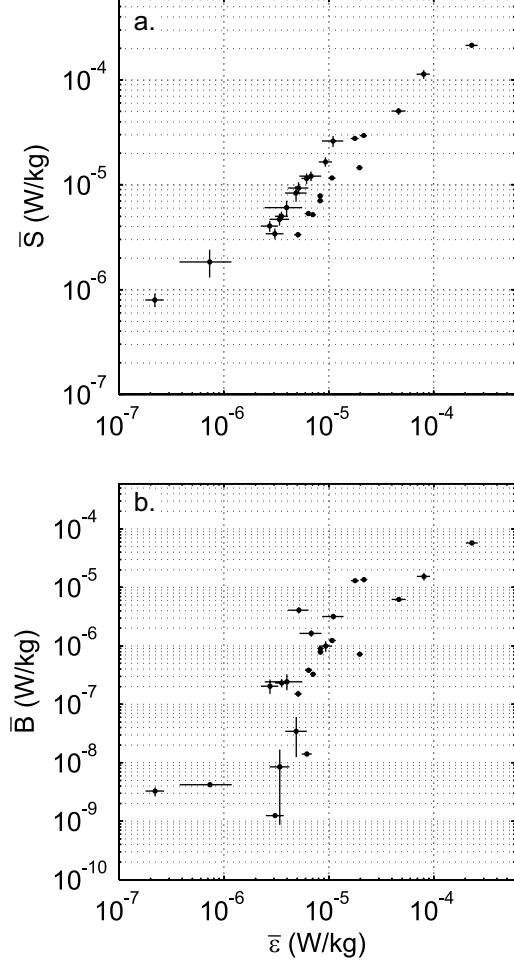


Fig. 9. (a) Comparison of estimated shear production,  $S = \frac{u_*^3}{\kappa|z|} \Phi_m$ , to the dissipation rate,  $\epsilon$ , for the deployment averages. (b) The dissipation rate generally increases with the local buoyancy conversion,  $B = g\alpha\langle w'T' \rangle$ . Turbulent heat flux relates to the buoyancy conversion by a factor of  $(\rho c_p)/(g\alpha)$ , which is a function of fluid temperature, but is approximately  $3 \times 10^9$  kg/m<sup>2</sup>. Ninety-five percent bootstrap confidence limits are shown for each estimate as a representation of the uncertainty.

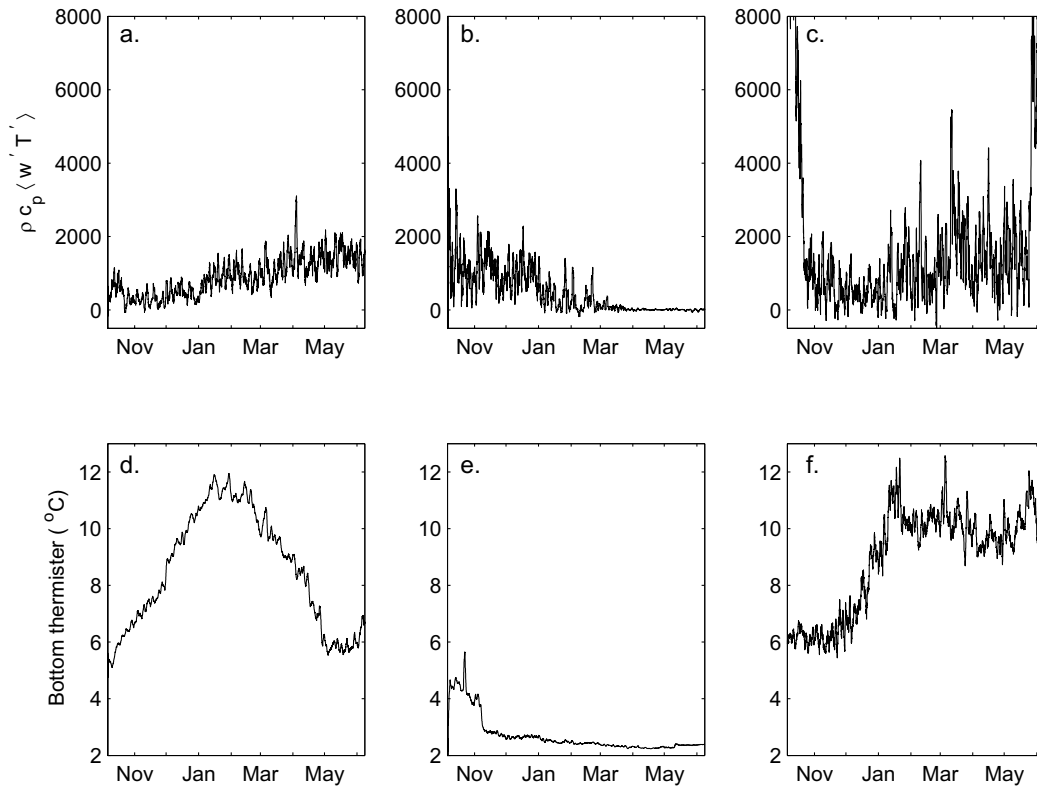


Fig. 10. Examples of turbulent heat fluxes (in  $\text{W/m}^2$ ) calculated for two instruments (a), (b) in the Clam Bed vent field and one (c) in the Easter Island vent area in Main Endeavour Field. The temperature recorded at each instrument base is shown in (d), (e) and (f), respectively. Instruments were deployed in 2000 and recovered in 2001. Data shown after a low-pass 36-h filter was applied for clarity. Large changes in temperature at the water / rock interface do not necessarily correspond to changes in the measured heat flux at 0.51 meters above the vent source.

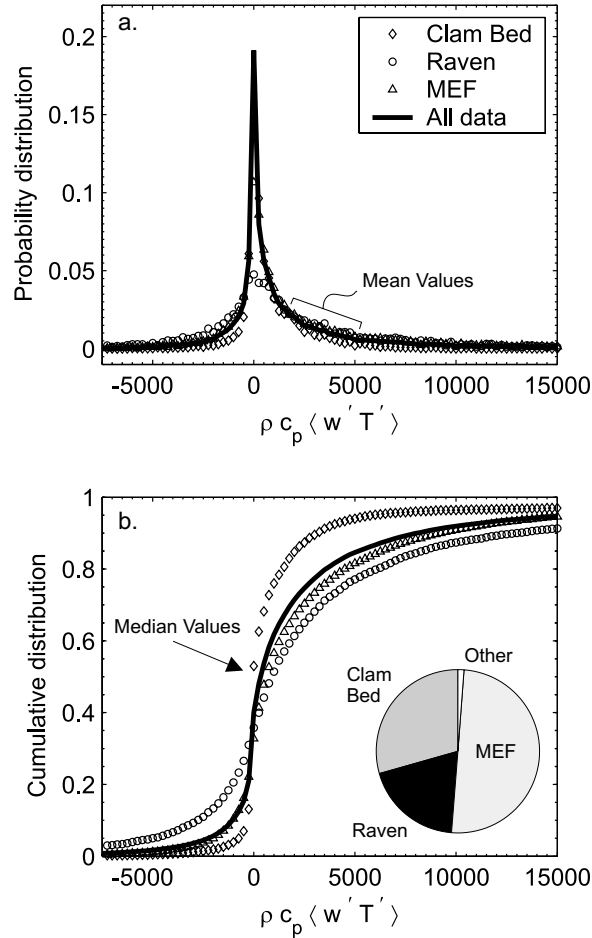


Fig. 11. (a) Probability distribution of turbulent heat flux estimates obtained during the 2000, 2001 and 2002 field programs. Large skewness is due to the efficiency with which heat is dispersed by larger eddies. (b) The large kurtosis, or peaked-ness, indicates that most of the actual heat transfer takes place during intermittent events. The median values for these observations range between 50–730  $\text{W/m}^2$ , while mean values are between 1800–5500  $\text{W/m}^2$ . The inset pie chart shows the spatial distribution of the measured heat flux values; 50% Main Endeavour Field, 19% Raven, 29% Clam Bed and  $<2\%$  in the central valley and High Rise vent field. Total number of observations over the three years was 36150 at twenty-five different locations, and the mean heat flux was 4100  $\text{W/m}^2$ .